JACS
JOURNAL OF THE AMERICAN CHEMICAL SOCIETY
pubs.acs.org/JACS
Article

Butterfly Effects Arising from Starting Materials in Fused-Ring Electron Acceptors

Tengfei Li, Yao Wu, Jiadong Zhou, Mengyang Li, Jingnan Wu, Qin Hu, Boyu Jia, Xiran Pan, Maojie Zhang, Zheng Tang, Zengqi Xie, Thomas P. Russell, and Xiaowei Zhan*

Cite This: https://dx.doi.org/10.1021/jacs.0c09800
Read Online

ABSTRACT: We designed and synthesized a series of fused-ring electron acceptors (FREAs) based on naphthalene-fused octacyclic cores end-capped by 3-(1,1-dicyanomethylene)-5,6-difluoro-1- indanone (NOICs) using a bottom-up approach. The NOIC series shares the same end groups and side chains, as well as similar fused-ring cores. The butterfly effects, arising from different methoxy positions in the starting materials, impact the design of the final FREAs, as well as their molecular packing, optical and electronic properties, charge transport, film morphology, and performance of organic solar cells. The binary-blend devices based on this NOIC series show power conversion efficiencies varying from 7.15% to 14.1%, due to the different intrinsic properties of the NOIC series, morphologies of blend films, and voltage losses of devices.

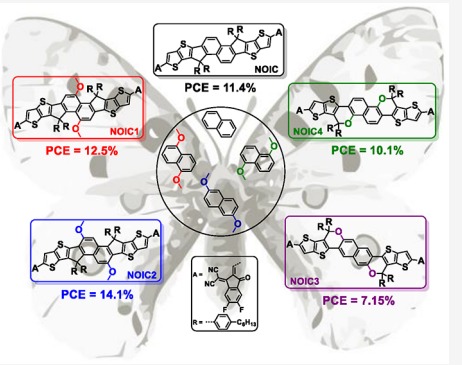

INTRODUCTION

Organic solar cells (OSCs) have the advantages of being lightweight, flexible, semitransparent, and printable over large-areas from solution and hold promise for building integrated photovoltaics, wearable devices, and indoor photovoltaics.[1,2] The photoactive layers of OSCs consist of electron donor and acceptor materials. In the past 3 decades, there has been a tremendous amount of research focusing on the development of high-performance photovoltaic materials.[2,3] Since we introduced the star molecule ITIC[4] and pioneered the concept of fused-ring electron acceptors (FREAs), FREAs have developed significantly and have dominated the area of acceptor materials.[5−14] FREAs have the desirable characteristics of easy molecular tailoring, tunability of energy levels, and strong absorption in the visible and near-infrared (NIR) regions, due to their modular acceptor−donor−acceptor (A−D−A) structure. The optical and electronic properties, crystallinity, film morphology, and photovoltaic performance of FREAs can be tuned by engineering the fused-ring cores,[13,15−27] end-capping groups,[28−38] and side chains.[6,39−44]

According to Shockley−Queisser limitation, extending optical absorption and reducing energy loss can improve efficiencies of OSCs. To realize improvement of device performance, rational design of molecular structures and precise modulation of properties of organic photovoltaic materials are essential but challenging. Nowadays, molecular design of FREAs generally adopts a top-down strategy that emphasizes the final molecular structure of FREAs, overlooking the starting materials and synthesis process. However, subtle changes on the starting materials may significantly perturb the chemical structures, physical properties, and photovoltaic performance of the resultant FREAs. For instance, when replacing the carbon-bridge in IDIC[6] with carbon−oxygen bridge, two isomers are formed due to the different oxygen positions, which significantly affect the PCEs of the devices (1.97% vs 10.42%).[45]

Here, we present a bottom-up approach for the rational design of high-performance FREAs and investigate the effects of the starting materials on molecular structures and properties of FREAs. We choose 2,6-bis(4,4,5,5-tetramethyl-1,3,2-dioxaborolan-2-yl)naphthalene and its methoxylated isomers as starting materials to synthesize a series of FREAs, NOICs (Chart 1). The NOIC series of molecules share the same end-capping groups and side chains, as well as similar fused-ring cores, but show different single crystal structures, absorption spectra, energy levels, and electron mobilities. The binary-blend OSCs based on the NOIC series and PM6[46] (Figure S1) have PCEs ranging from 7.15% to 14.1%. These results indicate that the butterfly effects resulting from small differences in the starting materials significantly affect the properties of the final FREAs, underscoring the need for bottom-up design for high-performance FREAs.

Received: September 13, 2020

Chart 1. Chemical Structures of SM1−4 and NOIC Series

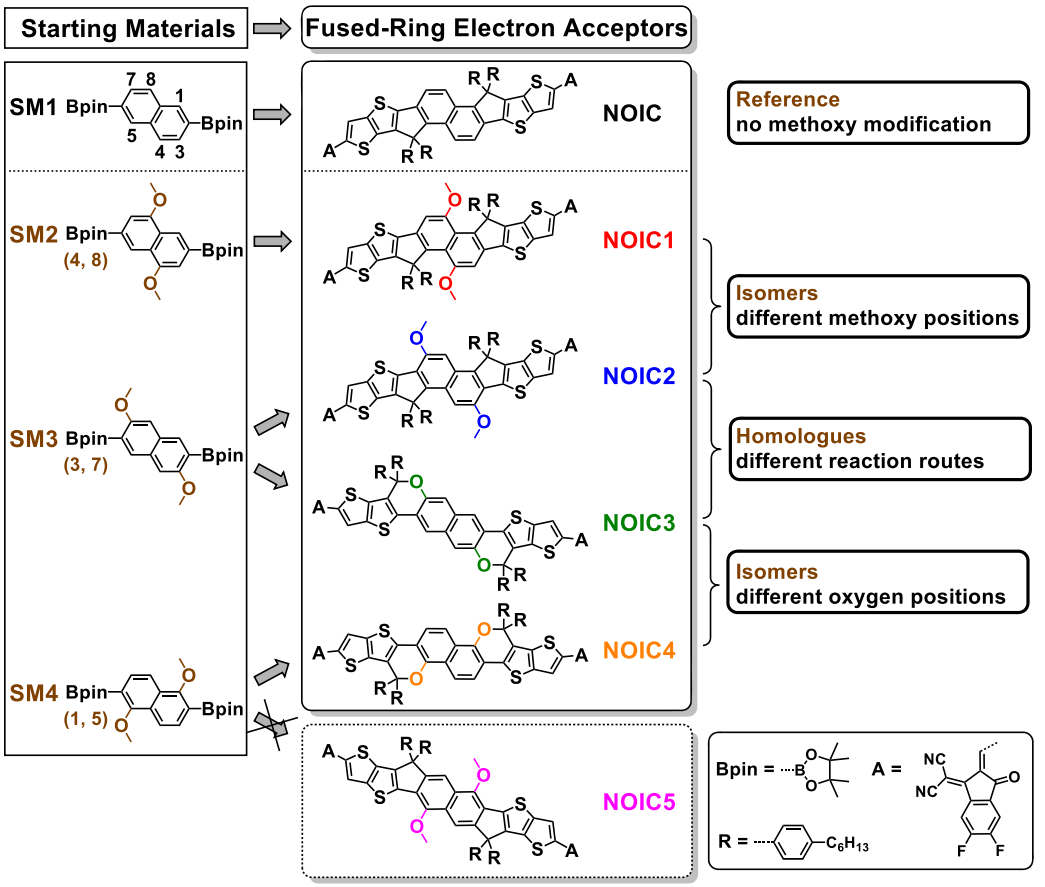

RESULTS AND DISCUSSION

Synthesis. The syntheses of the NOIC series are illustrated in Schemes 1 and S1−S7. First, we designed and synthesized NOIC by the Suzuki coupling reaction between starting material SM1 and ethyl 2-bromothieno[3,2-*b*]thiophene-3-carboxylate (TT-AB),[20] a nucleophilic addition, intramolecular Friedel−Crafts cyclization, Vilsmeier−Haack reaction, and Knoevenagel condensation with 3-(1,1-dicyanomethylene)-5,6-difluoro-1-indanone (2FIC)[31] in sequence (Scheme S2). To probe the butterfly effects in FREAs resulting from the different methoxy positions in starting materials, we substituted SM1 with three isomers SM2−4 where the methoxy position changed (Chart 1, Scheme 1). Theoretically, five FREAs (NOIC1−5) can be obtained, among which NOIC1 and NOIC2 are isomers with different methoxy positions; NOIC2 and NOIC3 are homologues from different reaction routes with the same starting material SM3; NOIC3 and NOIC4 are isomers with different oxygen positions; NOIC4 and NOIC5 are homologues from different reaction routes with the same starting material SM4.

The syntheses of NOIC1 and NOIC2 are similar to that of NOIC. Unlike NOIC1 and NOIC2, NOIC5 was not synthesized, since no target compound **13** was obtained after the regular nucleophilic addition reaction (Scheme S7). On the other hand, NOIC3 and NOIC4 are synthesized using SM3 and SM4 as starting materials, respectively, after the following reactions: Suzuki coupling reaction with TT-AB, demethylation reaction, acid-promoted intramolecular transesterification, nucleophilic addition, intramolecular dehydration cyclization, Vilsmeier−Haack reaction, and Knoevenagel condensation with 2FIC (Schemes S5 and S6).

Characterization. Molecules in the NOIC series have good solubility in chloroform and *o*-dichlorobenzene at room temperature and good thermal stability with decomposition temperatures at 5% weight loss (T_d) over 330 °C in nitrogen, as determined by thermogravimetric analysis (TGA) (Figure S2, Table 1).

The single crystal data and structural refinement of the NOIC series are given in Tables S1 and S2. All compounds have planar and rigid A−D−A backbones, due to the S···O interactions between the outermost thiophene in the "D" units and the carbonyl group in the "A" units. The intramolecular S···O interactions are shown in Figure S3 with distances of ∼2.7 Å for the D−A fragments of NOIC series. In addition, the S···O interactions in the core with a distance of 3.09 Å are observed for NOIC2. For the stacking patterns shown in Figure 1, NOIC has a 3D conjugated framework, due to the intermolecular $\pi-\pi$ interactions of adjacent D−A moieties (including 2FIC and partial core skeleton) analogous to other FREAs reported elsewhere. Introduction of methoxy groups at different positions leads to different conformations and, therefore, packing arrangements. Methoxy groups at the (4,8) positions seem to intensify the disorder of alkyl chains, causing four independent molecular conformations in the unit cell. NOIC1 shows $\pi-\pi$ stacking in directions orthogonal to the molecular long axis, leading to less overlap of the molecular backbone, a low packing index of 45.7%, and a large void percentage of 41.70%. Methoxy groups at the (3,7) positions introduce conformational locks by multiple S···O interactions, which are conducive to a planarity and rigidity of A−D−A skeleton. Although the stacking framework of NOIC2 is similar to that of NOIC, the stacking

https://dx.doi.org/10.1021/jacs.0c09800
J. Am. Chem. Soc. XXXX, XXX, XXX−XXX

Scheme 1. Synthetic Routes for NOIC Series

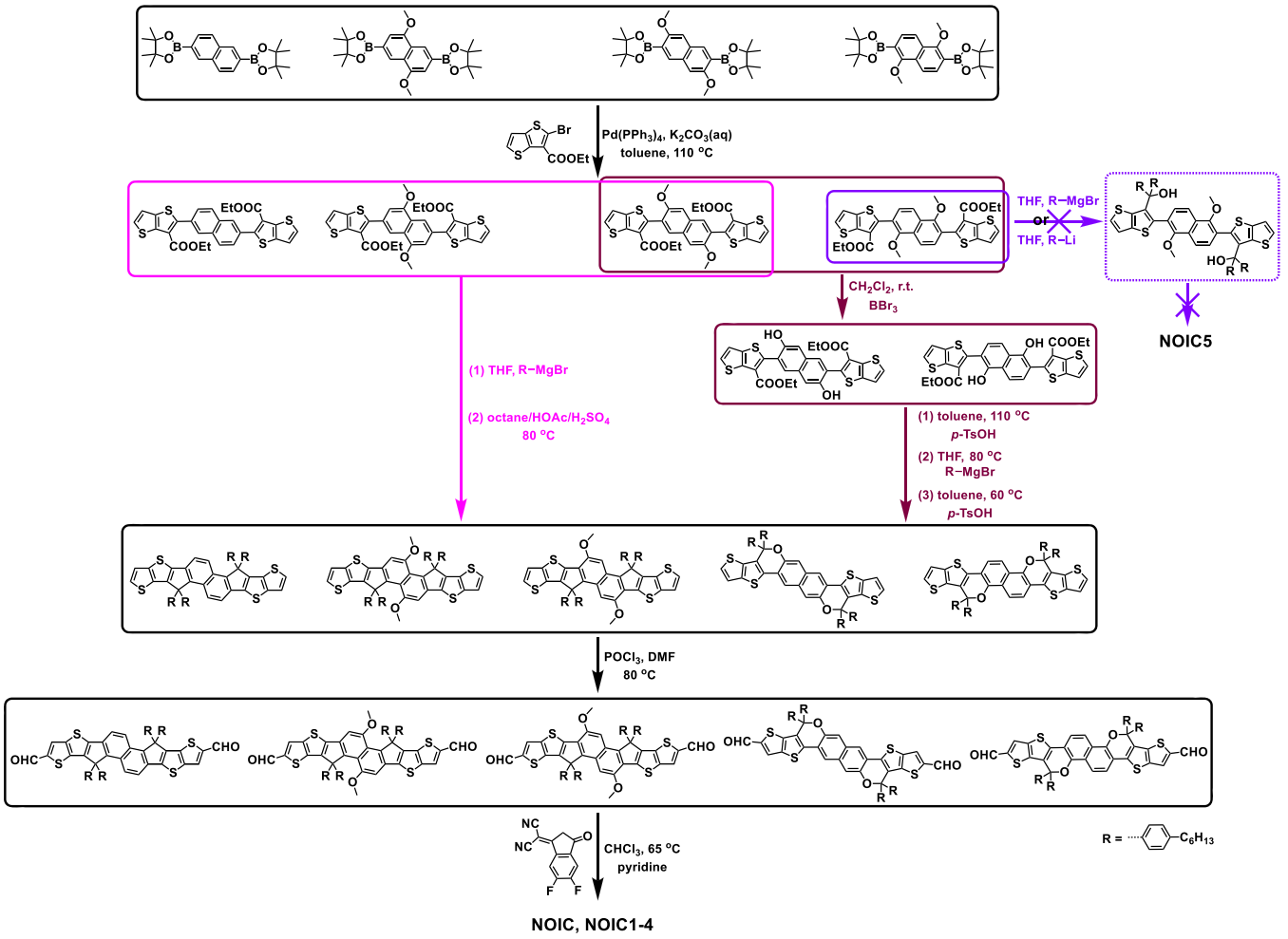

Table 1. Basic Properties of NOIC Series

		solution		film				
acceptor	T_d (°C)	λ_{max} (nm)	ε (10^5 M^{-1} cm^{-1})	λ_{max} (nm)	E_g^{opt} (eV)	HOMO (eV)	LUMO (eV)	μ_e (10^{-4} cm^2 V^{-1} s^{-1})
NOIC	344	687	2.5	722	1.55	−5.76	−4.03	6.2
NOIC1	336	762	2.4	802	1.38	−5.41	−4.02	7.1
NOIC2	336	702	2.1	748	1.49	−5.64	−3.99	9.0
NOIC3	340	644	2.0	668	1.62	−5.83	−3.95	0.66
NOIC4	352	687	2.4	730	1.55	−5.64	−3.90	1.2

of 2FIC fragments increases, which is beneficial for charge transport and exciton migration. As for NOIC3, the covalent cyclization of oxygen disrupts the coplanarity of the fused ring system and the steric crowding of the alkyl chains results in more complicated stacking pattern. Though fibrous crystals of NOIC4 were obtained, they are unstable, and crystal structure data could not be obtained.

The ordering of the neat NOIC films was investigated by grazing-incidence wide-angle X-ray scattering (GIWAXS). 2D GIWAXS profiles and related 1D plots are shown in Figure S4. NOIC is highly crystalline and shows two different crystal forms in the film. Both crystal forms show multiple orders of reflections with primary reflections at 0.31 $Å^{-1}$ (d = 20.3 Å) and 0.46 $Å^{-1}$ (d = 13.7 Å) in the in-plane direction. NOIC1 and NOIC2 are also highly crystalline, with primary reflections at 0.45 $Å^{-1}$ (d = 14.0 Å) and 0.46 $Å^{-1}$ (d = 13.7 Å), respectively, along with two higher order reflections in the in-plane direction. All the reflections of NOIC1 and NOIC2 are similar, indicating that the different methoxy positions have negligible effect on the packing. This is not consistent with single-crystal data where differences are observed, which may result from different conditions of crystal growth. NOIC3 and NOIC4 are slightly crystalline, showing only weak (100) reflections at 0.30 $Å^{-1}$ (d = 20.9 Å) and 0.35 $Å^{-1}$ (d = 18.0 Å) in the in-plane direction, respectively. All the NOIC series of acceptors have a face-on orientation in the film. The $\pi-\pi$ stacking peaks of the NOIC series are 1.80 $Å^{-1}$, 1.84 $Å^{-1}$, 1.84 $Å^{-1}$, 1.61 $Å^{-1}$, and 1.71 $Å^{-1}$ in the out-of-plane direction. The corresponding packing distance is 3.49 Å, 3.41 Å, 3.41 Å, 3.90 Å, and 3.67 Å.

The optical absorption data of the NOIC series are summarized in Table 1. In $CHCl_3$ solution (~10^{-6} M), NOIC series compounds show similar maximum molar extinction coefficients (ε) of (2−2.5) × 10^5 M^{-1} cm^{-1} but notably different peak absorption wavelengths (Figure S5a). In comparison to

https://dx.doi.org/10.1021/jacs.0c09800
J. Am. Chem. Soc. XXXX, XXX, XXX−XXX

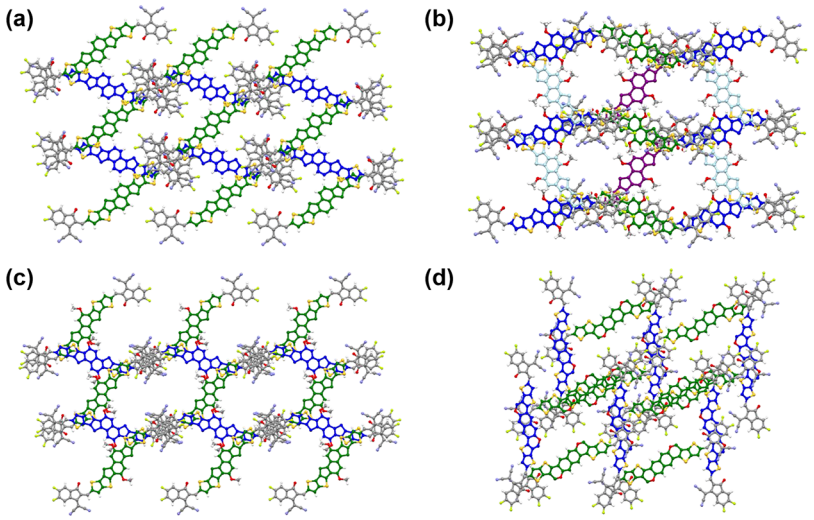

Figure 1. Molecular stacking patterns of (a) NOIC, (b) NOIC1, (c) NOIC2, and (d) NOIC3 in the crystal structures.

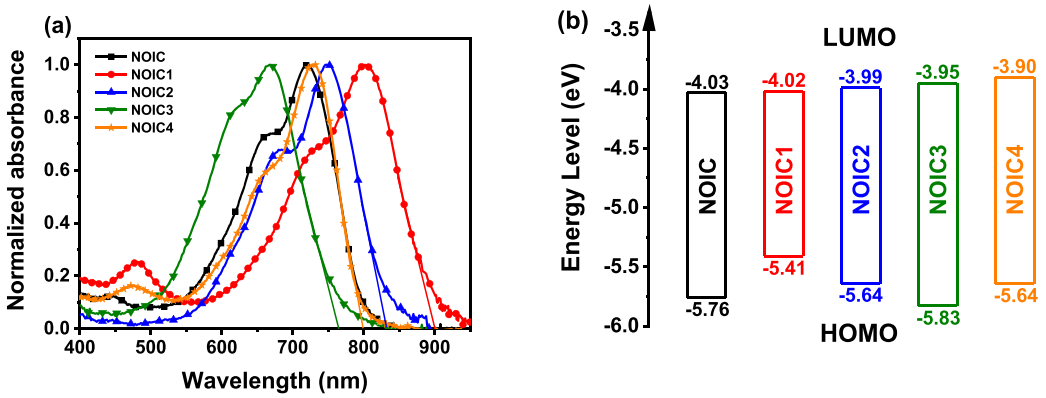

Figure 2. (a) Absorption spectra of NOIC series as thin films. (b) Energy levels of NOIC series.

NOIC (λ_{max} = 687 nm), the absorption peaks of NOIC1 and NOIC2 red-shift to 762 and 702 nm, respectively, due to the electron-donating effects of methoxy groups on the fused-ring cores. The peak of NOIC3 blue-shifts to 644 nm, while that of NOIC4 is the same as that of NOIC. The absorption peaks of $CHCl_3$-cast thin films red-shift 24−46 nm relative to those in solutions (Figure 2a). The optical bandgaps (E_g^{opt} values) of the NOIC series films are 1.38−1.62 eV, calculated from their absorption edges. Relative to methoxylated NOIC1 and NOIC2, NOIC3 and NOIC4 with carbon−oxygen bridges show blue-shifted absorption and larger bandgaps.

Electrochemical properties of the NOIC series were measured by cyclic voltammetry (CV) (Figure S6). In comparison to NOIC (LUMO/HOMO: −4.03/−5.76 eV), NOIC1 and NOIC2 exhibit similar LUMO levels (−4.02 eV and −3.99 eV) but higher HOMO levels (−5.41 eV and −5.64 eV), due to the electron-donating effects of the methoxy groups on the fused-ring cores. NOIC3 shows a higher LUMO (−3.95 eV) and a lower HOMO level (−5.83 eV), while NOIC4 shows higher LUMO and HOMO levels of −3.90 eV and −5.64 eV, respectively. Relative to the methoxylated NOIC1 and NOIC2, NOIC3 and NOIC4, with carbon−oxygen bridges, show higher LUMO energy levels.

Electron transport properties normal to the surface of films of the NOIC series were investigated by the space charge limited current (SCLC)[47] method (Figure S7). Compared to NOIC (6.2×10^{-4} cm^2 V^{-1} s^{-1}), NOIC1 and NOIC2 have slightly higher electron mobilities ($\mu_e = (7.1–9.0) \times 10^{-4}$ cm^2 V^{-1} s^{-1}), while NOIC3 and NOIC4 have significantly lower mobilities ($(0.66–1.2) \times 10^{-4}$ cm^2 V^{-1} s^{-1}). The higher electron mobilities of NOIC, NOIC1, and NOIC2 are due to the denser molecular packing in the films, as indicated by GIWAXS. Relative to the methoxylated NOIC1 and NOIC2, NOIC3 and NOIC4 with carbon−oxygen bridges show lower electron mobilities (Table 1).

Photovoltaic Performance. The widely used donor material PM6 has strong absorption in the 400−650 nm region (Figure S1b), complementing that of the NOIC series of acceptors, and has energy levels that align well with those of the NOIC series of acceptors. Hence, photovoltaic devices with an inverted structure of ITO/ZnO/active layer/MoO_3/Ag using PM6:NOIC series blends as photoactive layers were fabricated. Devices prepared from films of PM6 and the different NOICs (1:1 weight ratio) dissolved in $CHCl_3$ containing 0.2 vol % of 1,8-diiodooctane (DIO) as an additive spin-coated and annealed at 110 °C for 10 min showed the best performance (Figure S8, Table S3).

PM6:NOIC-based devices had an open-circuit voltage (V_{OC}) of 0.885 V, short-circuit current density (J_{SC}) of 18.1 mA cm^{-2}, fill factor (FF) of 71.2%, and PCE of 11.4% (Figure 3a, Table 2). Due to the red-shifted and broadened absorption (Figure S5b), PM6:NOIC1-based devices showed a notably enhanced J_{SC} of

https://dx.doi.org/10.1021/jacs.0c09800
J. Am. Chem. Soc. XXXX, XXX, XXX−XXX

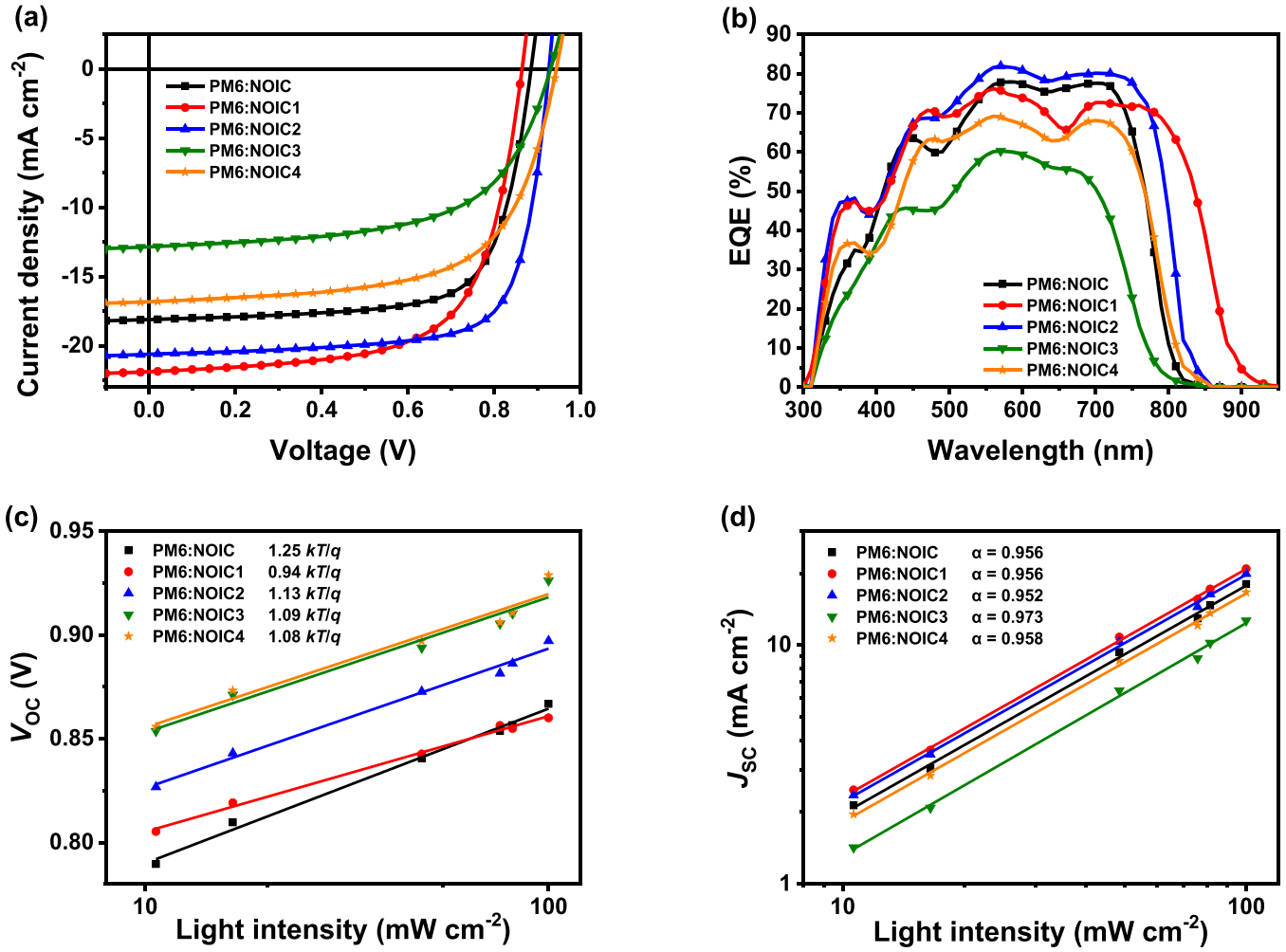

Figure 3. Photovoltaic performance of optimal OSCs based on PM6:NOIC series: (a) $J-V$ characteristics, (b) EQE spectra, (c) V_{OC} versus light intensity, and (d) J_{SC} versus light intensity.

Table 2. Device Data of Optimal OSCs Based on PM6:NOIC Series (1:1, w/w)

						μ (10^{-4} cm^2 V^{-1} s^{-1})		
acceptor[a]	V_{OC}[b] (V)	J_{SC}[b] (mA cm^{-2})	FF[b] (%)	PCE[b] (%)	calcd J_{SC} (mA cm^{-2})	μ_h	μ_e	μ_h/μ_e
NOIC	0.880 ± 0.007 (0.885)	17.7 ± 0.3 (18.1)	70.3 ± 0.6 (71.2)	11.0 ± 0.1 (11.4)	17.9	1.5	1.1	1.4
NOIC1	0.863 ± 0.004 (0.864)	21.1 ± 0.7 (21.9)	66.9 ± 1.6 (65.9)	12.2 ± 0.1 (12.5)	21.1	2.3	2.4	0.96
NOIC2	0.919 ± 0.005 (0.927)	20.2 ± 0.3 (20.6)	73.4 ± 0.7 (73.8)	13.6 ± 0.2 (14.1)	20.4	2.5	2.5	1.0
NOIC3	0.925 ± 0.006 (0.930)	12.6 ± 0.4 (12.9)	58.4 ± 1.2 (59.8)	6.81 ± 0.17 (7.15)	12.3	0.12	0.34	0.35
NOIC4	0.931 ± 0.007 (0.944)	16.6 ± 0.4 (16.8)	62.2 ± 1.3 (63.7)	9.63 ± 0.23 (10.1)	16.4	0.38	0.86	0.44

[a]0.2% DIO with thermal annealing at 110 °C for 10 min. [b]Average values with standard deviation were obtained from 20 devices, and values in parentheses are from the best devices.

21.9 mA cm^{-2} with a V_{OC} of 0.864 V and FF of 65.9%, yielding a higher PCE of 12.5%. Due to the red-shifted absorption and a higher μ_e of NOIC2, PM6:NOIC2-based devices had a higher J_{SC} of 20.6 mA cm^{-2} and FF of 73.8% and a V_{OC} of 0.927 V, yielding the highest PCE of 14.1%. Due to the blue-shifted absorption and a lower μ_e of NOIC3, PM6:NOIC3-based devices showed a dramatically reduced J_{SC} of 12.9 mA cm^{-2} and FF of 59.8% with a V_{OC} of 0.930 V, yielding a PCE of only 7.15%. Devices based on PM6:NOIC4 had a PCE of 10.1% with a V_{OC} of 0.944 V, J_{SC} of 16.8 mA cm^{-2}, and FF of 63.7%. Relative to methoxylated NOIC1 and NOIC2, NOIC3 and NOIC4 with carbon–oxygen bridges yielded much lower PCEs.

The external quantum efficiency (EQE) spectra of the best-performing devices based on PM6:NOIC series (Figure 3b) resemble absorption spectra of the blend films (Figure S5b). In comparison with PM6:NOIC-based devices with a maximum EQE value (EQE_{max}) of 78%, PM6:NOIC1 has a similar EQE_{max} of 76%, PM6:NOIC2 shows a higher EQE_{max} of 82%, while PM6:NOIC3 and PM6:NOIC4 show much lower EQE_{max} values of 60% and 69%. The J_{SC} values calculated by integrating the EQE spectra with the AM 1.5G reference spectrum are close to those obtained from $J-V$ measurements (Table 2).

The charge generation/extraction properties were studied by measuring the photocurrent density (J_{ph}) as a function of the effective voltage (V_{eff}) (Figure S9).[48] Theoretically, at a high V_{eff}

https://dx.doi.org/10.1021/jacs.0c09800
J. Am. Chem. Soc. XXXX, XXX, XXX−XXX

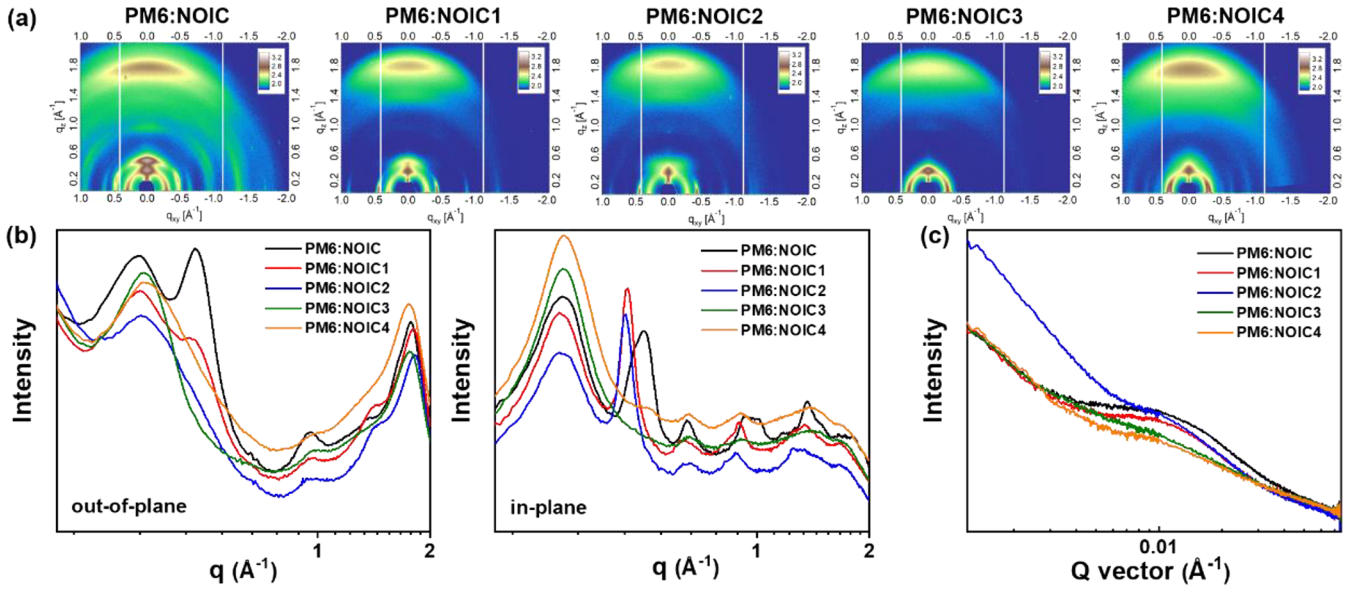

Figure 4. (a) 2D GIWAXS patterns, (b) scattering profiles of out-of-plane and in-plane, and (c) RSoXS profiles in log scale for PM6:NOIC series blend films.

(2.35 V), the saturation photocurrent density (J_{sat}) is only limited by the amount of photons absorbed in the active layer. Therefore, the ratio between J_{SC} and J_{sat} reflects the charge extraction efficiency under short-circuit conditions. The devices based on PM6:NOIC3 show a J_{SC}/J_{sat} of 0.916, which is lower than those of the other devices (0.943−0.958).

The charge recombination properties were evaluated by investigating V_{OC} and J_{SC} under different illumination intensities (P_{light}). The relationship between V_{OC} and P_{light} can be described as $V_{OC} \propto \ln(P_{light})$. The predominant types of recombination in the devices could be deduced from the slope values: k_BT/q for bimolecular recombination, $2k_BT/q$ for monomolecular recombination, and $0.5k_BT/q$ for surface recombination (k_B is the Boltzmann constant, T is temperature, and q is the elementary charge).[49−51] The slopes for the solar cells based on the NOIC series of acceptors are in the range between 0.94 and 1.25 k_BT/q, suggesting that bimolecular recombination is dominant in all devices (Figure 3c). The relationship between J_{SC} and P_{light} can be described as $J_{SC} \propto P_{light}^{\alpha}$, where $\alpha = 1$ implies negligible bimolecular recombination losses for the solar cell under a short circuit condition.[52] We find that all of the devices show similar α values (0.952−0.973), regardless of the acceptors used, indicating weak bimolecular recombination losses (Figure 3d).

The charge transport properties of PM6:NOIC series blend films were measured by the SCLC method (Figure S10). The PM6:NOIC blend film shows hole mobility (μ_h) of 1.5×10^{-4} cm^2 V^{-1} s^{-1} and μ_e of 1.1×10^{-4} cm^2 V^{-1} s^{-1} with a μ_h/μ_e ratio of 1.4; PM6:NOIC1 and PM6:NOIC2 blend films show higher and more balanced mobilities ($\mu_h = (2.3–2.5) \times 10^{-4}$ cm^2 V^{-1} s^{-1}; $\mu_e = (2.4–2.5) \times 10^{-4}$ cm^2 V^{-1} s^{-1}; μ_h/μ_e = 0.96−1.0), which benefit the J_{SC} and FF; PM6:NOIC3 and PM6:NOIC4 blend films show lower and less balanced mobilities ($\mu_h = (0.12–0.38) \times 10^{-4}$ cm^2 V^{-1}; $\mu_e = (0.34–0.86) \times 10^{-4}$ cm^2 V^{-1}; μ_h/μ_e = 0.35−0.44), leading to lower J_{SC} and FF (Table 2).

Stability of the PM6:NOIC series-based devices was investigated under illumination or heating conditions without encapsulation in a glovebox with inert atmosphere (Figure S11). Under AM 1.5G illumination at 100 mW cm^{-2} for 180 min, PCEs of PM6:NOIC1- and PM6:NOIC2-based devices remained at 89.4% and 95.2% of their initial values, respectively, which are better than that of PM6:NOIC based devices (82.5%), while PM6:NOIC3- and PM6:NOIC4-based devices showed poorer stability with PCEs decaying to 49.9% and 55.2% of the initial values, respectively. With heating at 100 °C for 180 min, the PCEs of PM6:NOIC1- and PM6:NOIC2-based devices remained at 97.1% and 93.8% of the initial values, respectively, which are better than that of PM6:NOIC based devices (91.2%), while PM6:NOIC3- and PM6:NOIC4-based devices showed poorer stability, with PCEs decaying to 84.1% and 78.3% of the initial values, respectively. Relative to methoxylated NOIC1 and NOIC2, NOIC3 and NOIC4 with carbon−oxygen bridges showed worse thermal stability and photostability of the devices.

Film Morphology. The surface morphology of PM6:NOIC series blend films was investigated by atomic force microscopy (AFM) (Figure S12). The blend films have similar root-mean-square roughnesses of 4.00−4.62 nm. The molecular packing and orientation behavior of blend films were explored by GIWAXS (Figure 4). The donor PM6 shows a (100) peak at 0.32 Å^{-1} in both the in-plane and out-of-plane directions with a preferred edge-on orientation (Figure S4). The (100) peak of PM6 in the out-of-plane direction remains when blended with the NOIC series of acceptors. It is difficult to define a preferred orientation of PM6 when blended with NOIC, NOIC3, and NOIC4, since the (100) reflections at ∼0.30 Å^{-1} of NOIC, NOIC3, and NOIC4 merge together with the (100) peak of PM6 in the in-plane direction. PM6 remains edge-on when blended with NOIC1 and NOIC2. The strong (100) peaks of the acceptors are located at 0.50 Å^{-1}, 0.45 Å^{-1}, and 0.44 Å^{-1} in PM6:NOIC, PM6:NOIC1, and PM6:NOIC2 blend films, respectively. The corresponding coherent lengths, determined from a Scherrer analysis, are 8.7 nm, 19.1 nm, and 17.8 nm, which are all larger than those in pure films (8.0 nm, 17.2 nm, and 15.2 nm), indicating PM6 can induce an ordering of these three acceptors in the blend films. The relatively larger coherent lengths of NOIC1 and NOIC2 benefit electron transport in the acceptor phase. The $\pi-\pi$ stacking peaks of PM6:NOIC series are located at 1.78 Å^{-1}, 1.80 Å^{-1}, 1.82 Å^{-1}, 1.76 Å^{-1}, and 1.76 Å^{-1} (d = 3.53 Å, 3.49 Å, 3.45 Å, 3.57 Å, and 3.57 Å) in the out-of-

https://dx.doi.org/10.1021/jacs.0c09800
J. Am. Chem. Soc. XXXX, XXX, XXX−XXX

Table 3. Detailed V_{OC} Losses of Optimal OSCs Based on PM6:NOIC Series

acceptor	V_{OC} (V)	E_g^{PV} (eV)	E_{CT} (eV)	EQE_{EL}	ΔE_{CT} (eV)	ΔV_{nonrad} (V)	ΔV_{rad} (V)	V_{loss} (V)
NOIC	0.89	1.62	1.38	1.18×10^{-5}	0.24	0.28	0.21	0.73
NOIC1	0.86	1.46	1.36	1.24×10^{-4}	0.10	0.22	0.28	0.60
NOIC2	0.93	1.57	1.44	1.61×10^{-5}	0.13	0.28	0.23	0.64
NOIC3	0.93	1.70	1.45	2.20×10^{-5}	0.25	0.27	0.25	0.77
NOIC4	0.94	1.62	1.49	4.54×10^{-5}	0.13	0.25	0.30	0.68

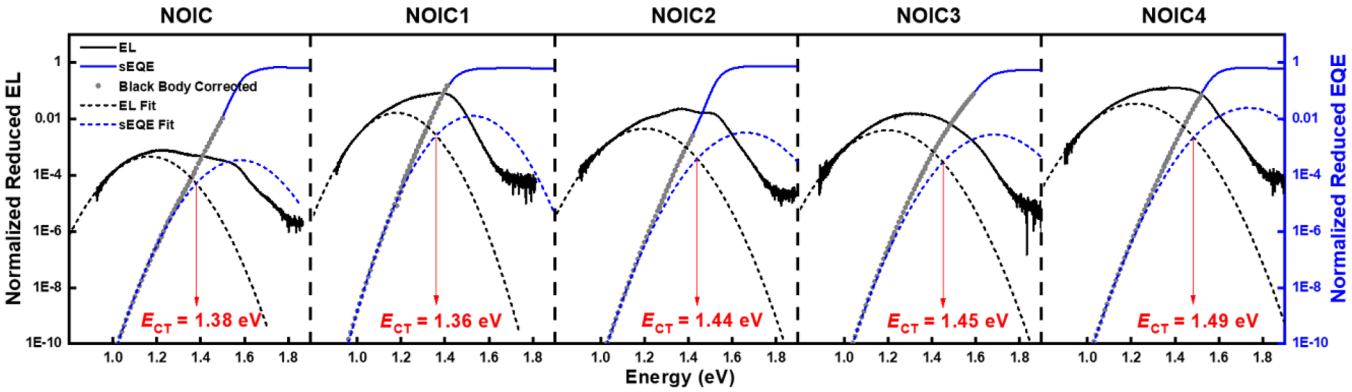

Figure 5. Reduced EL and EQE spectra of optimal OSCs based on PM6:NOIC series.

plane direction, respectively. The smaller $\pi-\pi$ packing distances facilitate charge transport in the PM6:NOIC1 and PM6:NOIC2 blends, resulting in better performance of the devices.

Resonant soft X-ray scattering (RSoXS) was used to investigate the morphology of PM6:NOIC series blend films.[53,54] To enhance contrast, an energy at the carbon edge of 285.0 eV was used. The scattering peaks of PM6:NOIC, PM6:NOIC1, and PM6:NOIC2 located at 0.0099 $Å^{-1}$, 0.0097 $Å^{-1}$, and 0.0103 $Å^{-1}$ correspond to average mesh sizes of 31.6 nm, 32.4 nm, and 30.5 nm, respectively (Figure 4c). This mesh arises from a network-like arrangement of the fibrillar crystals of the acceptor in a mixed donor−acceptor matrix. Well-defined interferences are seen for PM6:NOIC, PM6:NOIC1, and PM6:NOIC2, indicating the establishments of a well-defined crystalline network of the acceptors which is beneficial for charge transport and corresponds to the better performance. The interference seen for PM6:NOIC2 is better characterized as a shoulder on the monotonically decreasing scattering seen at smaller scattering vectors for all systems, suggesting a better mixing between PM6 and NOIC2, thus hindering crystallization. This is the origin of the smaller coherent length for PM6:NOIC2 in the GIWAXS.[55] No obvious scattering interferences were evident for PM6:NOIC3 and PM6:NOIC4 blend films, suggesting a suppression of the formation of a well-defined network structure due to the mixing between the donor and acceptor. From the GIWAXS data, it is evident that well-defined crystal reflections are seen for the entire NOIC series. Consequently, it is not the crystalline ordering that is dominantly affected by the donor−acceptor mixing but rather the arrangements of the crystalline fibrils in the mixed donor−acceptor matrix. This crystalline network is important for charge transport, and as such, a disruption of the network will lead to recombination losses or traps that will detrimentally influence performance.

Voltage Loss. To understand the differences in V_{OC} (0.86−0.94 V), we examined V_{loss} in the solar cells based on the PM6:NOICs.[56−58] The total voltage loss can be divided into three parts according to the equation S2 (Supporting Information): the voltage loss due to charge generation ($\Delta E_{CT}/q$), the nonradiative recombination voltage loss (ΔV_{nonrad}), and the voltage loss due to radiative recombination (ΔV_{rad}). Detailed values are given in Table 3.

ΔE_{CT} is defined as the difference between the energy of the bandgap of the blend film (E_g^{PV}) and the energy of the charge transfer (CT) state (E_{CT}). In this work, E_g^{PV} is determined from the crossing point between the normalized photoluminescence (PL) and absorption spectra of the neat acceptor film, because the acceptor has a lower bandgap compared to that of PM6 (Figure S13). Furthermore, E_{CT} is determined by fitting to the low energy part of sensitive EQE (sEQE) spectra, using methods described previously in the literature (Figure 5).[57,59] From these measurements, we find that, in comparison to NOIC and NOIC3 (ΔE_{CT} = 0.24−0.25 eV), NOIC1-, NOIC2-, and NOIC4-based devices have notably smaller ΔE_{CT} (0.10−0.13 eV), indicating smaller driving force for charge transfer in these devices. However, devices based on NOIC2, NOIC3, and NOIC4 have a higher E_{CT} (1.44−1.49 eV), compared to the devices based on NOIC and NOIC1, which is the main reason for the higher V_{OC} (0.93−0.94 V).

The electroluminescence external quantum efficiencies (EQE_{EL}) of the solar cells are also measured, as shown in Figure S14, and ΔV_{nonrad} values, calculated according to equation S2, are listed in Table 3.[56] The EQE_{EL} is 1.24×10^{-4} for NOIC1-based device, leading to the smallest ΔV_{nonrad} of 0.22 V, while the devices based on the other acceptors have relatively larger ΔV_{nonrad} of 0.25−0.28 V. ΔV_{rad} is calculated using equation S2, and we find that NOIC-based devices have the smallest ΔV_{rad} of 0.21 V. NOIC2- and NOIC3-based devices have higher ΔV_{rad} (0.23 and 0.25 V, respectively), while the highest values of 0.28 and 0.30 V are obtained for NOIC1- and NOIC4-based devices. Finally, in comparison with NOIC-based devices (V_{loss} = 0.73 V), NOIC1- and NOIC2-based devices exhibit notably smaller V_{loss} of 0.60 and 0.64 V, respectively, due to the much smaller ΔE_{CT}. The small but sufficient driving force for charge transfer in the solar cell is beneficial for device performance. Although NOIC3- and NOIC4-based devices

https://dx.doi.org/10.1021/jacs.0c09800
J. Am. Chem. Soc. XXXX, XXX, XXX−XXX

exhibit relatively higher V_{OC}, the high ΔE_{CT} for NOIC3 and high ΔV_{rad} for NOIC4 result in too high V_{loss} of 0.77 and 0.68 V, respectively, partially responsible for the low PCEs of devices. The different losses discussed here can also be related to the formation or lack of formation of a well-defined network of crystals, as discussed earlier, arising from the extent of mixing of the donor and acceptor.

CONCLUSIONS

We designed five NOIC series molecules and synthesized from starting materials SM1 and its three methoxylated isomers SM2−4. The NOIC series has the same end groups and side chains as well as similar fused-ring cores but shows different molecular packing, light absorption, energy levels, and electron mobilities. The binary-blend OSCs based on the NOIC series show notably different PCEs varying from 7.15% to 14.1%, due to the different properties of NOICs, morphology of blend films, and voltage losses of devices. NOIC2-based devices have the highest PCE of 14.1%. This study reveals that the butterfly effects arising from the different methoxy positions in the starting materials significantly affect properties of FREAs. (i) Methoxy substitution on the fused-ring core is beneficial for red-shifted absorption, stronger crystallinity, higher charge mobility, lower voltage loss, higher device efficiency, and better stability, while carbon−oxygen bridge show negative effects. (ii) The methoxylation position and oxygen heterocyclization position have significant impact on molecular packing, absorption, energy levels, electron mobilities, film morphology, and photovoltaic performance of FREAs. These results indicate that minor changes on the starting materials could significantly affect the chemical structures, physical properties, and photovoltaic performance of the resultant acceptors. The often-used top-down design emphasizes the final molecular structure but ignores the starting materials and synthesis process and may be insufficient for rational design. The bottom-up strategy is important for designing high-performance nonfullerene acceptors and should be taken into account.

ASSOCIATED CONTENT

Supporting Information

The Supporting Information is available free of charge at https://pubs.acs.org/doi/10.1021/jacs.0c09800.

Detailed experimental procedures including synthesis, characterization, device fabrication, and additional characterization data, such as TGA, single crystals, GIWAXS, absorption spectra, CV, SCLC, AFM, PL spectra, EQE_{EL}, and optimization and stability of the OSC devices (PDF)

Single-crystal structures of NOIC (2031646), NOIC1 (2031647), NOIC2 (2031648), and NOIC3 (2031649) (CIF)

AUTHOR INFORMATION

Corresponding Author

Xiaowei Zhan − *Department of Materials Science and Engineering, College of Engineering, Key Laboratory of Polymer Chemistry and Physics of Ministry of Education, Peking University, Beijing 100871, China;* orcid.org/0000-0002-1006-3342; Email: xwzhan@pku.edu.cn

Authors

Tengfei Li − *Department of Materials Science and Engineering, College of Engineering, Key Laboratory of Polymer Chemistry and Physics of Ministry of Education, Peking University, Beijing 100871, China;* orcid.org/0000-0002-0501-1505

Yao Wu − *Department of Polymer Science and Engineering, University of Massachusetts Amherst, Amherst, Massachusetts 01003, United States;* orcid.org/0000-0002-6680-7347

Jiadong Zhou − *Institute of Polymer Optoelectronic Materials and Devices, State Key Laboratory of Luminescent Materials and Devices, South China University of Technology, Guangzhou 510640, China*

Mengyang Li − *Center for Advanced Low-Dimension Materials, State Key Laboratory for Modification of Chemical Fibers and Polymer Materials, College of Materials Science and Engineering, Donghua University, Shanghai 201620, China*

Jingnan Wu − *Laboratory of Advanced Optoelectronic Materials, College of Chemistry, Chemical Engineering and Materials Science, Soochow University, Suzhou 215123, China*

Qin Hu − *Department of Polymer Science and Engineering, University of Massachusetts Amherst, Amherst, Massachusetts 01003, United States; Materials Sciences Division, Lawrence Berkeley National Laboratory, Berkeley, California 94720, United States*

Boyu Jia − *Department of Materials Science and Engineering, College of Engineering, Key Laboratory of Polymer Chemistry and Physics of Ministry of Education, Peking University, Beijing 100871, China*

Xiran Pan − *Department of Materials Science and Engineering, College of Engineering, Key Laboratory of Polymer Chemistry and Physics of Ministry of Education, Peking University, Beijing 100871, China*

Maojie Zhang − *Laboratory of Advanced Optoelectronic Materials, College of Chemistry, Chemical Engineering and Materials Science, Soochow University, Suzhou 215123, China;* orcid.org/0000-0002-6102-5856

Zheng Tang − *Center for Advanced Low-Dimension Materials, State Key Laboratory for Modification of Chemical Fibers and Polymer Materials, College of Materials Science and Engineering, Donghua University, Shanghai 201620, China;* orcid.org/0000-0003-0036-2362

Zengqi Xie − *Institute of Polymer Optoelectronic Materials and Devices, State Key Laboratory of Luminescent Materials and Devices, South China University of Technology, Guangzhou 510640, China;* orcid.org/0000-0003-0826-840X

Thomas P. Russell − *Department of Polymer Science and Engineering, University of Massachusetts Amherst, Amherst, Massachusetts 01003, United States; Materials Sciences Division, Lawrence Berkeley National Laboratory, Berkeley, California 94720, United States;* orcid.org/0000-0001-6384-5826

Complete contact information is available at: https://pubs.acs.org/10.1021/jacs.0c09800

Notes

The authors declare no competing financial interest.

ACKNOWLEDGMENTS

X.Z. thanks the NSFC (Grants 21734001 and 51761165023). T.P.R. and Y.W. are supported by the U.S. Office of Naval Research under Contract N00014-17-1-2244. Portions of this research were conducted at beamlines 7.3.3 and 11.0.1.2 of

https://dx.doi.org/10.1021/jacs.0c09800
J. Am. Chem. Soc. XXXX, XXX, XXX−XXX

Advanced Light Source, Materials Science Division, The Molecular Foundry, Lawrence Berkeley National Laboratory, which was supported by the Office of Science, Office of Basic Energy Sciences, of the U.S. Department of Energy under Contract No. DE-AC02-05CH11231. Z.X. thanks the NSFC (Grants 21733005 and 51761135101).

REFERENCES

(1) Lu, L.; Zheng, T.; Wu, Q.; Schneider, A. M.; Zhao, D.; Yu, L. Recent advances in bulk heterojunction polymer solar cells. *Chem. Rev.* **2015**, *115* (23), 12666−12731.

(2) Cheng, P.; Li, G.; Zhan, X.; Yang, Y. Next-generation organic photovoltaics based on non-fullerene acceptors. *Nat. Photonics* **2018**, *12* (3), 131−142.

(3) Li, Y. Molecular design of photovoltaic materials for polymer solar cells: Toward suitable electronic energy levels and broad absorption. *Acc. Chem. Res.* **2012**, *45* (5), 723−733.

(4) Lin, Y.; Wang, J.; Zhang, Z. G.; Bai, H.; Li, Y.; Zhu, D.; Zhan, X. An electron acceptor challenging fullerenes for efficient polymer solar cells. *Adv. Mater.* **2015**, *27* (7), 1170−1174.

(5) Yan, C.; Barlow, S.; Wang, Z.; Yan, H.; Jen, A. K.-Y.; Marder, S. R.; Zhan, X. Non-fullerene acceptors for organic solar cells. *Nat. Rev. Mater.* **2018**, *3* (3), 18003.

(6) Lin, Y.; He, Q.; Zhao, F.; Huo, L.; Mai, J.; Lu, X.; Su, C. J.; Li, T.; Wang, J.; Zhu, J.; Sun, Y.; Wang, C.; Zhan, X. A facile planar fused-ring electron acceptor for as-cast polymer solar cells with 8.71% efficiency. *J. Am. Chem. Soc.* **2016**, *138* (9), 2973−2976.

(7) Zhao, W.; Qian, D.; Zhang, S.; Li, S.; Inganas, O.; Gao, F.; Hou, J. Fullerene-free polymer solar cells with over 11% efficiency and excellent thermal stability. *Adv. Mater.* **2016**, *28* (23), 4734−4739.

(8) Zhou, Z.; Xu, S.; Song, J.; Jin, Y.; Yue, Q.; Qian, Y.; Liu, F.; Zhang, F.; Zhu, X. High-efficiency small-molecule ternary solar cells with a hierarchical morphology enabled by synergizing fullerene and non-fullerene acceptors. *Nat. Energy* **2018**, *3* (11), 952−959.

(9) Meng, L.; Zhang, Y.; Wan, X.; Li, C.; Zhang, X.; Wang, Y.; Ke, X.; Xiao, Z.; Ding, L.; Xia, R.; Yip, H.-L.; Cao, Y.; Chen, Y. Organic and solution-processed tandem solar cells with 17.3% efficiency. *Science* **2018**, *361* (6407), 1094−1098.

(10) Li, X.; Pan, F.; Sun, C.; Zhang, M.; Wang, Z.; Du, J.; Wang, J.; Xiao, M.; Xue, L.; Zhang, Z. G.; Zhang, C.; Liu, F.; Li, Y. Simplified synthetic routes for low cost and high photovoltaic performance n-type organic semiconductor acceptors. *Nat. Commun.* **2019**, *10* (1), 519.

(11) Cheng, P.; Liu, Y.; Chang, S.-Y.; Li, T.; Sun, P.; Wang, R.; Cheng, H.-W.; Huang, T.; Meng, L.; Nuryyeva, S.; Zhu, C.; Wei, K.-H.; Sun, B.; Zhan, X.; Yang, Y. Efficient tandem organic photovoltaics with tunable rear sub-cells. *Joule* **2019**, *3* (2), 432−442.

(12) Xu, X.; Zhang, G.; Yu, L.; Li, R.; Peng, Q. P3ht-based polymer solar cells with 8.25% efficiency enabled by a matched molecular acceptor and smart green-solvent processing technology. *Adv. Mater.* **2019**, *31* (52), 1906045.

(13) Yuan, J.; Zhang, Y. Q.; Zhou, L. Y.; Zhang, G. C.; Yip, H. L.; Lau, T. K.; Lu, X. H.; Zhu, C.; Peng, H. J.; Johnson, P. A.; Leclerc, M.; Cao, Y.; Ulanski, J.; Li, Y. F.; Zou, Y. P. Single-junction organic solar cell with over 15% efficiency using fused-ring acceptor with electron-deficient core. *Joule* **2019**, *3* (4), 1140−1151.

(14) Liu, Q.; Jiang, Y.; Jin, K.; Qin, J.; Xu, J.; Li, W.; Xiong, J.; Liu, J.; Xiao, Z.; Sun, K.; Yang, S.; Zhang, X.; Ding, L. 18% efficiency organic solar cells. *Sci. Bull.* **2020**, *65* (4), 272−275.

(15) Wang, W.; Yan, C.; Lau, T. K.; Wang, J.; Liu, K.; Fan, Y.; Lu, X.; Zhan, X. Fused hexacyclic nonfullerene acceptor with strong near-infrared absorption for semitransparent organic solar cells with 9.77% efficiency. *Adv. Mater.* **2017**, *29* (31), 1701308.

(16) Kan, B.; Feng, H.; Wan, X.; Liu, F.; Ke, X.; Wang, Y.; Wang, Y.; Zhang, H.; Li, C.; Hou, J.; Chen, Y. Small-molecule acceptor based on the heptacyclic benzodi(cyclopentadithiophene) unit for highly efficient nonfullerene organic solar cells. *J. Am. Chem. Soc.* **2017**, *139* (13), 4929−4934.

(17) Li, T.; Dai, S.; Ke, Z.; Yang, L.; Wang, J.; Yan, C.; Ma, W.; Zhan, X. Fused tris(thienothiophene)-based electron acceptor with strong near-infrared absorption for high-performance as-cast solar cells. *Adv. Mater.* **2018**, *30* (10), 1705969.

(18) Xiao, Z.; Jia, X.; Li, D.; Wang, S.; Geng, X.; Liu, F.; Chen, J.; Yang, S.; Russell, T. P.; Ding, L. 26 mA cm^{-2} J_{SC} from organic solar cells with a low-bandgap nonfullerene acceptor. *Sci. Bull.* **2017**, *62* (22), 1494−1496.

(19) Dai, S.; Li, T.; Wang, W.; Xiao, Y.; Lau, T. K.; Li, Z.; Liu, K.; Lu, X.; Zhan, X. Enhancing the performance of polymer solar cells via core engineering of NIR-absorbing electron acceptors. *Adv. Mater.* **2018**, *30* (15), 1706571.

(20) Wang, J.; Zhang, J.; Xiao, Y.; Xiao, T.; Zhu, R.; Yan, C.; Fu, Y.; Lu, G.; Lu, X.; Marder, S. R.; Zhan, X. Effect of isomerization on high-performance nonfullerene electron acceptors. *J. Am. Chem. Soc.* **2018**, *140* (29), 9140−9147.

(21) Liu, W.; Zhang, J.; Zhou, Z.; Zhang, D.; Zhang, Y.; Xu, S.; Zhu, X. Design of a new fused-ring electron acceptor with excellent compatibility to wide-bandgap polymer donors for high-performance organic photovoltaics. *Adv. Mater.* **2018**, *30* (26), 1800403.

(22) Li, S.; Zhan, L.; Liu, F.; Ren, J.; Shi, M.; Li, C. Z.; Russell, T. P.; Chen, H. An unfused-core-based nonfullerene acceptor enables high-efficiency organic solar cells with excellent morphological stability at high temperatures. *Adv. Mater.* **2018**, *30* (6), 1705208.

(23) Zhu, J.; Ke, Z.; Zhang, Q.; Wang, J.; Dai, S.; Wu, Y.; Xu, Y.; Lin, Y.; Ma, W.; You, W.; Zhan, X. Naphthodithiophene-based nonfullerene acceptor for high-performance organic photovoltaics: Effect of extended conjugation. *Adv. Mater.* **2018**, *30* (2), 1704713.

(24) Sun, J.; Ma, X.; Zhang, Z.; Yu, J.; Zhou, J.; Yin, X.; Yang, L.; Geng, R.; Zhu, R.; Zhang, F.; Tang, W. Dithieno[3,2-b:2′,3′-d]pyrrol fused nonfullerene acceptors enabling over 13% efficiency for organic solar cells. *Adv. Mater.* **2018**, *30* (16), 1707150.

(25) Yao, Z.; Liao, X.; Gao, K.; Lin, F.; Xu, X.; Shi, X.; Zuo, L.; Liu, F.; Chen, Y.; Jen, A. K. Dithienopicenocarbazole-based acceptors for efficient organic solar cells with optoelectronic response over 1000 nm and an extremely low energy loss. *J. Am. Chem. Soc.* **2018**, *140* (6), 2054−2057.

(26) Chen, T.-W.; Peng, K.-L.; Lin, Y.-W.; Su, Y.-J.; Ma, K.-J.; Hong, L.; Chang, C.-C.; Hou, J.; Hsu, C. S. A chlorinated nonacyclic carbazole-based acceptor affords over 15% efficiency in organic solar cells. *J. Mater. Chem. A* **2020**, *8* (3), 1131−1137.

(27) Jia, B.; Wang, J.; Wu, Y.; Zhang, M.; Jiang, Y.; Tang, Z.; Russell, T. P.; Zhan, X. Enhancing the performance of a fused-ring electron acceptor by unidirectional extension. *J. Am. Chem. Soc.* **2019**, *141* (48), 19023−19031.

(28) Lin, Y.; Zhang, Z.-G.; Bai, H.; Wang, J.; Yao, Y.; Li, Y.; Zhu, D.; Zhan, X. High-performance fullerene-free polymer solar cells with 6.31% efficiency. *Energy Environ. Sci.* **2015**, *8* (2), 610−616.

(29) Wu, Y.; Bai, H.; Wang, Z.; Cheng, P.; Zhu, S.; Wang, Y.; Ma, W.; Zhan, X. A planar electron acceptor for efficient polymer solar cells. *Energy Environ. Sci.* **2015**, *8* (11), 3215−3221.

(30) Li, S.; Ye, L.; Zhao, W.; Zhang, S.; Mukherjee, S.; Ade, H.; Hou, J. Energy-level modulation of small-molecule electron acceptors to achieve over 12% efficiency in polymer solar cells. *Adv. Mater.* **2016**, *28* (42), 9423−9429.

(31) Dai, S.; Zhao, F.; Zhang, Q.; Lau, T. K.; Li, T.; Liu, K.; Ling, Q.; Wang, C.; Lu, X.; You, W.; Zhan, X. Fused nonacyclic electron acceptors for efficient polymer solar cells. *J. Am. Chem. Soc.* **2017**, *139* (3), 1336−1343.

(32) Tang, A.; Xiao, B.; Wang, Y.; Gao, F.; Tajima, K.; Bin, H.; Zhang, Z.-G.; Li, Y.; Wei, Z.; Zhou, E. Simultaneously achieved high open-circuit voltage and efficient charge generation by fine-tuning charge-transfer driving force in nonfullerene polymer solar cells. *Adv. Funct. Mater.* **2018**, *28* (6), 1704507.

(33) Feng, H.; Qiu, N.; Wang, X.; Wang, Y.; Kan, B.; Wan, X.; Zhang, M.; Xia, A.; Li, C.; Liu, F.; Zhang, H.; Chen, Y. An A-D-A type small-molecule electron acceptor with end-extended conjugation for high performance organic solar cells. *Chem. Mater.* **2017**, *29* (18), 7908−7917.

https://dx.doi.org/10.1021/jacs.0c09800
J. Am. Chem. Soc. XXXX, XXX, XXX−XXX

(34) Yao, H.; Cui, Y.; Yu, R.; Gao, B.; Zhang, H.; Hou, J. Design, synthesis, and photovoltaic characterization of a small molecular acceptor with an ultra-narrow band gap. *Angew. Chem., Int. Ed.* **2017**, *56* (11), 3045−3049.
(35) Liu, Y.; Zhang, Z.; Feng, S.; Li, M.; Wu, L.; Hou, R.; Xu, X.; Chen, X.; Bo, Z. Exploiting noncovalently conformational locking as a design strategy for high performance fused-ring electron acceptor used in polymer solar cells. *J. Am. Chem. Soc.* **2017**, *139* (9), 3356−3359.
(36) Xie, D.; Liu, T.; Gao, W.; Zhong, C.; Huo, L.; Luo, Z.; Wu, K.; Xiong, W.; Liu, F.; Sun, Y.; Yang, C. A novel thiophene-fused ending group enabling an excellent small molecule acceptor for high-performance fullerene-free polymer solar cells with 11.8% efficiency. *Solar RRL* **2017**, *1* (6), 1700044.
(37) Aldrich, T. J.; Matta, M.; Zhu, W.; Swick, S. M.; Stern, C. L.; Schatz, G. C.; Facchetti, A.; Melkonyan, F. S.; Marks, T. J. Fluorination effects on indacenodithienothiophene acceptor packing and electronic structure, end-group redistribution, and solar cell photovoltaic response. *J. Am. Chem. Soc.* **2019**, *141* (7), 3274−3287.
(38) Luo, Z.; Ma, R.; Liu, T.; Yu, J.; Xiao, Y.; Sun, R.; Xie, G.; Yuan, J.; Chen, Y.; Chen, K.; Chai, G.; Sun, H.; Min, J.; Zhang, J.; Zou, Y.; Yang, C.; Lu, X.; Gao, F.; Yan, H. Fine-tuning energy levels via asymmetric end groups enables polymer solar cells with efficiencies over 17%. *Joule* **2020**, *4* (6), 1236−1247.
(39) Lin, Y.; Zhao, F.; He, Q.; Huo, L.; Wu, Y.; Parker, T. C.; Ma, W.; Sun, Y.; Wang, C.; Zhu, D.; Heeger, A. J.; Marder, S. R.; Zhan, X. High-performance electron acceptor with thienyl side chains for organic photovoltaics. *J. Am. Chem. Soc.* **2016**, *138* (14), 4955−4961.
(40) Yang, Y.; Zhang, Z. G.; Bin, H.; Chen, S.; Gao, L.; Xue, L.; Yang, C.; Li, Y. Side-chain isomerization on an n-type organic semiconductor itic acceptor makes 11.77% high efficiency polymer solar cells. *J. Am. Chem. Soc.* **2016**, *138* (45), 15011−15018.
(41) Wang, J.; Wang, W.; Wang, X.; Wu, Y.; Zhang, Q.; Yan, C.; Ma, W.; You, W.; Zhan, X. Enhancing performance of nonfullerene acceptors via side-chain conjugation strategy. *Adv. Mater.* **2017**, *29* (35), 1702125.
(42) Fei, Z.; Eisner, F. D.; Jiao, X.; Azzouzi, M.; Rohr, J. A.; Han, Y.; Shahid, M.; Chesman, A. S. R.; Easton, C. D.; McNeill, C. R.; Anthopoulos, T. D.; Nelson, J.; Heeney, M. An alkylated indacenodithieno[3,2-b]thiophene-based nonfullerene acceptor with high crystallinity exhibiting single junction solar cell efficiencies greater than 13% with low voltage losses. *Adv. Mater.* **2018**, *30* (8), 1705209.
(43) Li, Y.; Zheng, N.; Yu, L.; Wen, S.; Gao, C.; Sun, M.; Yang, R. A simple phenyl group introduced at the tail of alkyl side chains of small molecular acceptors: New strategy to balance the crystallinity of acceptors and miscibility of bulk heterojunction enabling highly efficient organic solar cells. *Adv. Mater.* **2019**, *31* (12), 1807832.
(44) Dai, S.; Zhou, J.; Chandrabose, S.; Shi, Y.; Han, G.; Chen, K.; Xin, J.; Liu, K.; Chen, Z.; Xie, Z.; Ma, W.; Yi, Y.; Jiang, L.; Hodgkiss, J. M.; Zhan, X. High-performance fluorinated fused-ring electron acceptor with 3D stacking and exciton/charge transport. *Adv. Mater.* **2020**, *32* (21), 2000645.
(45) Li, X.; Huang, H.; Peng, Z.; Sun, C.; Yang, D.; Zhou, J.; Liebman-Pelaez, A.; Zhu, C.; Zhang, Z.-G.; Zhang, Z.; Xie, Z.; Ade, H.; Li, Y. Effects of fused-ring regiochemistry on the properties and photovoltaic performance of n-type organic semiconductor acceptors. *J. Mater. Chem. A* **2018**, *6* (33), 15933−15941.
(46) Zhang, M.; Guo, X.; Ma, W.; Ade, H.; Hou, J. A large-bandgap conjugated polymer for versatile photovoltaic applications with high performance. *Adv. Mater.* **2015**, *27* (31), 4655−4660.
(47) Malliaras, G. G.; Salem, J. R.; Brock, P. J.; Scott, C. Electrical characteristics and efficiency of single-layer organic light-emitting diodes. *Phys. Rev. B: Condens. Matter Mater. Phys.* **1998**, *58* (20), No. R13411.
(48) Lu, L.; Xu, T.; Chen, W.; Landry, E. S.; Yu, L. Ternary blend polymer solar cells with enhanced power conversion efficiency. *Nat. Photonics* **2014**, *8* (9), 716−722.
(49) Koster, L. J. A.; Mihailetchi, V. D.; Ramaker, R.; Blom, P. W. M. Light intensity dependence of open-circuit voltage of polymer:-Fullerene solar cells. *Appl. Phys. Lett.* **2005**, *86* (12), 123509.
(50) Cowan, S. R.; Roy, A.; Heeger, A. J. Recombination in polymer-fullerene bulk heterojunction solar cells. *Phys. Rev. B: Condens. Matter Mater. Phys.* **2010**, *82* (24), 245207.
(51) Wheeler, S.; Deledalle, F.; Tokmoldin, N.; Kirchartz, T.; Nelson, J.; Durrant, J. R. Influence of surface recombination on charge-carrier kinetics in organic bulk heterojunction solar cells with nickel oxide interlayers. *Phys. Rev. Appl.* **2015**, *4* (2), No. 024020.
(52) Schilinsky, P.; Waldauf, C.; Brabec, C. J. Recombination and loss analysis in polythiophene based bulk heterojunction photodetectors. *Appl. Phys. Lett.* **2002**, *81* (20), 3885−3887.
(53) Liu, F.; Wang, C.; Baral, J. K.; Zhang, L.; Watkins, J. J.; Briseno, A. L.; Russell, T. P. Relating chemical structure to device performance via morphology control in diketopyrrolopyrrole-based low band gap polymers. *J. Am. Chem. Soc.* **2013**, *135* (51), 19248−19259.
(54) Liu, F.; Gu, Y.; Shen, X.; Ferdous, S.; Wang, H.-W.; Russell, T. P. Characterization of the morphology of solution-processed bulk heterojunction organic photovoltaics. *Prog. Polym. Sci.* **2013**, *38* (12), 1990−2052.
(55) Weng, K.; Ye, L.; Zhu, L.; Xu, J.; Zhou, J.; Feng, X.; Lu, G.; Tan, S.; Liu, F.; Sun, Y. Optimized active layer morphology toward efficient and polymer batch insensitive organic solar cells. *Nat. Commun.* **2020**, *11* (1), 2855.
(56) Benduhn, J.; Tvingstedt, K.; Piersimoni, F.; Ullbrich, S.; Fan, Y.; Tropiano, M.; McGarry, K. A.; Zeika, O.; Riede, M. K.; Douglas, C. J.; Barlow, S.; Marder, S. R.; Neher, D.; Spoltore, D.; Vandewal, K. Intrinsic non-radiative voltage losses in fullerene-based organic solar cells. *Nat. Energy* **2017**, *2* (6), 17053.
(57) Karki, A.; Vollbrecht, J.; Dixon, A. L.; Schopp, N.; Schrock, M.; Reddy, G. N. M.; Nguyen, T. Q. Understanding the high performance of over 15% efficiency in single-junction bulk heterojunction organic solar cells. *Adv. Mater.* **2019**, *31* (48), 1903868.
(58) Vandewal, K.; Tvingstedt, K.; Gadisa, A.; Inganäs, O.; Manca, J. V. Relating the open-circuit voltage to interface molecular properties of donor:Acceptor bulk heterojunction solar cells. *Phys. Rev. B: Condens. Matter Mater. Phys.* **2010**, *81* (12), 125204.
(59) Wang, Y.; Jia, B.; Wang, J.; Xue, P.; Xiao, Y.; Li, T.; Wang, J.; Lu, H.; Tang, Z.; Lu, X.; Huang, F.; Zhan, X. High-efficiency perovskite quantum dot hybrid nonfullerene organic solar cells with near-zero driving force. *Adv. Mater.* **2020**, *32* (29), 2002066.

https://dx.doi.org/10.1021/jacs.0c09800
J. Am. Chem. Soc. XXXX, XXX, XXX−XXX